

OPTIMIZING NON-INTERSECTING SYNTHETIC VASCULAR TREES IN NONCONVEX ORGANS

 **Etienne Jessen**

Institute for Mechanics, Computational Mechanics Group
Technical University of Darmstadt
64287 Darmstadt, Germany
etienne.jessen@tu-darmstadt.de

 **Marc C. Steinbach**

Institute of Applied Mathematics
Leibniz Universität Hannover
30167 Hannover, Germany
mcs@ifam.uni-hannover.de

 **Dominik Schillinger**

Institute for Mechanics, Computational Mechanics Group
Technical University of Darmstadt
64287 Darmstadt, Germany
dominik.schillinger@tu-darmstadt.de

ABSTRACT

Objective: The understanding of the mechanisms driving vascular development is still limited. Techniques to generate vascular trees synthetically have been developed to tackle this problem. However, most algorithms are limited to single trees inside convex perfusion volumes. We introduce a new framework for generating multiple trees inside general nonconvex perfusion volumes. *Methods:* Our framework combines topology optimization and global geometry optimization into a single algorithmic approach. Our first contribution is defining a baseline problem based on Murray's original formulation, which accommodates efficient solution algorithms. The problem of finding the global minimum is cast into a nonlinear optimization problem (NLP) with merely super-linear solution effort. Our second contribution extends the NLP to constrain multiple vascular trees inside any nonconvex boundary while avoiding intersections. We test our framework against a benchmark of an anatomic region of brain tissue and a vasculature of the human liver. *Results:* In all cases, the total tree energy is improved significantly compared to local approaches. *Conclusion:* By avoiding intersections globally, we can reproduce key physiological features such as parallel running inflow vessels and tortuous vessels. *Significance:* The ability to generate non-intersecting vascular trees inside nonconvex organs can improve the functional assessment of organs.

Keywords nonconvex organs · liver · brain · synthetic vascular trees · NLP

1 Introduction

The vasculature of the human body is responsible for supplying cells with nutrients by permitting blood to circulate throughout the body [1]. Here, vascular trees are responsible for either distributing (supplying) or collecting (draining) the blood to and from the micro-circulation. These trees are hierarchical and reach from the largest arteries and veins (10 cm) to the smallest arterioles/venules (50 μm) and are the target of many diseases, e.g., abdominal aneurysms [2] or stroke in the brain [3]. To this date, there is only limited understanding of how these diseases develop and how they can be detected early on. One major reason is that the understanding of what drives the development of vascular trees across the different scales and what constitutes a healthy vascular tree is still limited. Consequently, a better understanding could elevate the functional assessment of organs based on available (patient-specific) imaging data.

One promising idea to achieve a better understanding is to generate a vascular tree synthetically. This was first conceived by Schreiner [4] in 1993 and was later extended by Karch to three dimensions [5]. They used a method called Constrained Constructive Optimization (CCO) to generate trees iteratively by adding a new terminal node at each iteration. To this day most generation methods are based on CCO, and extensions were made to fit the method to specific organs, e.g., the liver [6–8], brain [9] or retina [10]. Some work also went into improving other aspects of the method, such as including nonconvex regions [11] or multiple trees [12]. However, to this day, CCO is still limited to local optimality principles. Alternative methods such as Global Constructive Optimization (GCO) [13] and Simulated Annealing [14] were developed as a response but are still based on local optimizations and suffer from poor computational complexity. Consequently, a quantitative comparison against real vascular trees remains a challenge. In [8], we used rigorous mathematical optimization methods to alleviate some of these problems by extending the algorithm to consider the global geometry and topology. In [15], we extended the model further to include a non-Newtonian blood model in the form of the Fåhræus–Lindqvist effect. However, during all studies, we only considered a single tree inside a perfusion domain without severe nonconvex features.

In this paper, we extend the framework introduced in [8, 15] to generate multiple non-intersecting vascular trees inside the same (generally nonconvex) perfusion volume. We utilize our global optimization framework to enforce non-intersection of all trees and containment inside the volume (semi-) globally. Lastly, we test our new approach for a brain region with severe nonconvexity and for the complete liver with three distinct vascular trees.

2 Methods

2.1 Definitions and assumptions

The perfusion domain of an organ of interest is denoted by Ω . We describe the topology of each vascular tree as a directed graph $\mathbb{T} = (\mathbb{V}, \mathbb{A})$ with nodes $u \in \mathbb{V}$ and segments $a \in \mathbb{A}$. The *root* (index 0) is the proximal node of the single root segment, and each node distal to a terminal segment is a *leave* $v \in \mathbb{L}$. The geometry of each tree consists of the geometric location x_u of each node u , and the length $\ell_a = \|x_u - x_v\|$, radius r_a and volumetric flow Q_a of each segment $a = uv$. A segment thus simplifies a *vessel* to a rigid and straight cylindrical tube, schematically shown in Fig. 1.

The blood flow through each vessel is assumed to be laminar and we approximate blood as an incompressible, homogeneous Newtonian fluid. Poiseuille’s law then describes the flow through each segment with

$$\Delta p_a = R_a Q_a \quad \forall a \in \mathbb{A}, \quad (1)$$

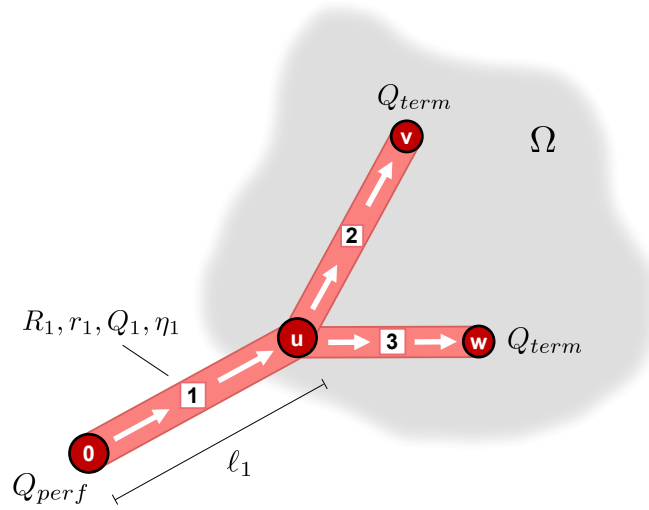


Figure 1: Schematic of a vascular tree and its relation to nodes and segments. Red circles denote a node, white rectangles denote a segment. This tree has a given inflow $Q_1 = Q_{\text{perf}}$ and equal terminal outflow $Q_2 = Q_3 = Q_{\text{term}}$ through each of the outlets (leaves). Arrows indicate the flow direction from the root node to the terminal nodes. All branching and terminal nodes are inside the (nonconvex) perfusion domain Ω .

where $\Delta p_a = p_u - p_v$ is the pressure drop across segment $a = uv$. The hydrodynamic resistance R_a of each segment a follows with

$$R_a = \frac{8\eta}{\pi} \frac{\ell_a}{r_a^4} \quad \forall a \in \mathbb{A}, \quad (2)$$

where η is the dynamic viscosity of blood. Each tree is perfused at steady-state by a given perfusion (root) flow Q_{perf} . We note that any (arbitrary) distribution of flow at the leaves can be modeled in our framework. A standard assumption is a homogeneous distribution of Q_{perf} to all N leaves, resulting in a terminal flow $Q_{\text{term}} = Q_{\text{perf}}/N$. In any case, Kirchhoff's law describes the flow distributions at the branching nodes with

$$Q_{uv} = \sum_{vw \in \mathbb{A}} Q_{vw} \quad \forall v \in \mathbb{V} \setminus (\{0\} \cup \mathbb{L}). \quad (3)$$

The trees are assumed to obey scaling relations based on minimizing certain cost functions. Murray [16] proposed that each vessel minimizes its total power, which consists of the power to maintain blood inside the vessel, P_{vol} , and the (viscous) power to move blood through the vessel, P_{vis} . The resulting scaling relation, known as Murray's law, describes the relationship between the radius of a parent vessel (r_0) and its children's vessels (r_1, \dots, r_n) with

$$r_0^3 = r_1^3 + \dots + r_n^3. \quad (4)$$

We extend Murray's formulation to the entire tree, which results in the cost function

$$f_{\mathbb{T}} = P_{\text{vol}} + P_{\text{vis}} = \sum_{a \in \mathbb{A}} m_b \pi \ell_a r_a^2 + \frac{8\eta}{\pi} \frac{\ell_a}{r_a^4} Q_a^2. \quad (5)$$

The parameter m_b is the metabolic demand of blood, measured in $\mu\text{W mm}^{-3}$. It describes the accumulated energy expenditure of blood (blood plasma and RBCs) and vessels. More details on this parameter can be found in [17].

2.2 Derivation of baseline problem

From these assumptions we derive an optimization problem that is used as the basis for our generation framework. We start by rewriting (5) to

$$f_{\mathbb{T}} = \sum_{a \in \mathbb{A}} \ell_a w_a(r_a), \quad (6)$$

where w_a is the power weight function defined at each segment a with given parameters m_b , η and Q_a ,

$$w_a(r_a) := w(r_a; m_b, \eta, Q_a) := m_b \pi r_a^2 + \frac{8\eta}{\pi r_a^4} Q_a^2. \quad (7)$$

Our assumptions do not include any global coupling constraints between nodes. As a result, the (globally) optimal radius of each segment a can be independently computed by solving

$$\frac{\partial w}{\partial r_a} = 2m_b \pi r_a - \frac{32\eta Q_a^2}{\pi r_a^5} = 0, \quad (8)$$

leading to

$$r_a = \sqrt[6]{\frac{16\eta}{m_b \pi^2} Q_a^2}. \quad (9)$$

Since we enforce conservation of mass at each branch with Kirchhoff's law (3), we satisfy Murray's law automatically. This is to be expected, as we derived our solution from his original problem. We note, though, that the validity of Murray's law depends on the type of optimization problem considered, as highlighted in [15]. By assuming a constant blood viscosity η and metabolic demand m_b , we can simplify (9) to

$$r_a = c_1 \sqrt[3]{Q_a} \quad \forall a \in \mathbb{A}, \quad c_1 := \sqrt[6]{\frac{16\eta}{m_b \pi^2}}. \quad (10)$$

If we further assume equal outflow, the flow across vessel a simply becomes

$$Q_a = Q_{uv} = Q_0 \frac{|\mathbb{L}_u|}{|\mathbb{L}_0|} \quad \forall a \in \mathbb{A}, \quad (11)$$

where $|\mathbb{L}_u|$ is the number of leaf nodes downstream of node u (with $\mathbb{L}_0 = \mathbb{L}$). In this case, the radius only depends on the topology of the tree with

$$r_a = r_{uv} = c_2 \sqrt[3]{|\mathbb{L}_u|} \quad \forall a \in \mathbb{A}, \quad c_2 = c_1 \sqrt[3]{\frac{Q_0}{|\mathbb{L}_0|}}. \quad (12)$$

Both c_1 and c_2 are constants that can be computed before starting our solution algorithm, based on the choice of flow distribution. The problem of finding the optimal geometry of a tree then only consists in finding the optimal nodal positions (and corresponding vessel lengths).

2.3 Geometry optimization

2.3.1 NLP formulation of global geometry

Current state-of-the-art generation methods for synthetic vascular trees, such as [9, 11], only perform a local optimization of each single branch point when ‘‘growing’’ the tree node by node. In [8], we extended this

process to cover the global geometry, which included the positions and pressures at all branching nodes as well as the lengths and radii of all arcs. The problem was cast into a nonlinear optimization problem (NLP), which admits efficient solution algorithms. Based on this approach, we now construct an NLP for our baseline problem. We note that various other design goals and constraints can also be modeled simply by adapting or extending our baseline problem.

As described in [8, 15] in more detail, we include all variables to be optimized in the vector y . For our baseline problem, this only includes the nodal positions $x = (x_v)_{v \in \mathbb{V}}$ and the vessel lengths $\ell = (\ell_a)_{a \in \mathbb{A}}$, giving the variable vector $y = (x, \ell) \in \mathbb{R}^{3|\mathbb{V}|+|\mathbb{A}|}$. We add a physical lower bound ℓ^- and, for numerical efficiency, an upper bound ℓ^+ . Because we do not generate the microcirculation, the lower bound ℓ^- is set to 0.01 mm. The upper bound ℓ^+ must be set based on the organ and should allow the largest possible vessels to form. Then, the best geometry is found in the rectangle defined as

$$Y = \mathbb{R}^{3|\mathbb{V}|} \times [\ell^-, \ell^+]^{|\mathbb{A}|}, \quad (13)$$

and the NLP reads:

$$\min_{y \in Y} \sum_{a \in \mathbb{A}} \ell_a w_a(r_a) \quad (14)$$

$$\text{s.t. } 0 = x_u - \bar{x}_u, \quad u \in \{0\} \cup \mathbb{L}, \quad (15)$$

$$0 = \ell_{uv}^2 - \|x_u - x_v\|^2, \quad uv \in \mathbb{A}. \quad (16)$$

Here (15) fixes the positions of the root node and the terminal nodes, and (16) ensures consistency between nodal positions and segment lengths. The effect of global geometry optimization by means of our NLP is illustrated in Fig. 2 where we synthesized the tree inside a shallow rectangular box with dimensions $100\text{mm} \times 100\text{mm} \times 20\text{mm}$ and with the root node located outside the bottom right corner. All figures show the projection to the xy -plane. The total energy expenditure of the original tree (based on (5)) is reduced by around 3% with our NLP approach. Furthermore, the global optimization straightens the “jagged” paths between segments, which arise as a consequence of repeated local optimizations.

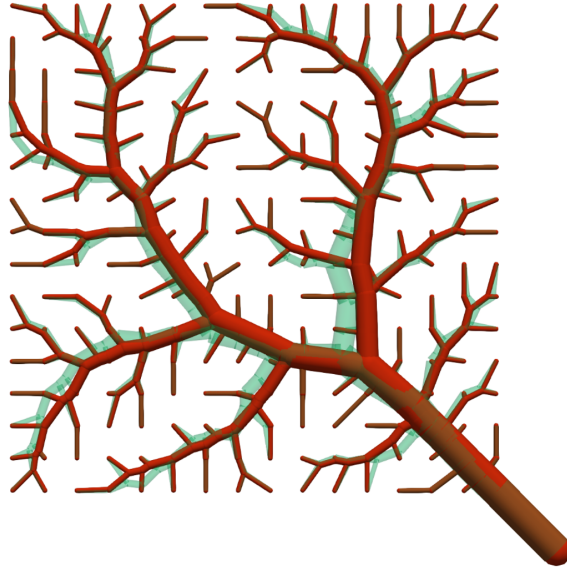


Figure 2: Comparison between local geometry optimization (green tree) and global geometry optimization (red tree) for 200 terminal nodes. Optimizing the global geometry reduces the total cost by about 3%.

2.3.2 Extension to nonconvex domains

The global geometry optimization works for any convex perfusion volume and more generally when the shortest weighted connections between two tree nodes are always inside Ω . However, nonconvex features such as holes may require further effort, as shown in Fig. 3 for a rectangle-shaped perfusion volume Ω (in grey). Even when terminal nodes are generated inside the nonconvex perfusion volume, both branching nodes and edges can lie partially or entirely outside the domain Ω (highlighted on the left of Fig. 3).

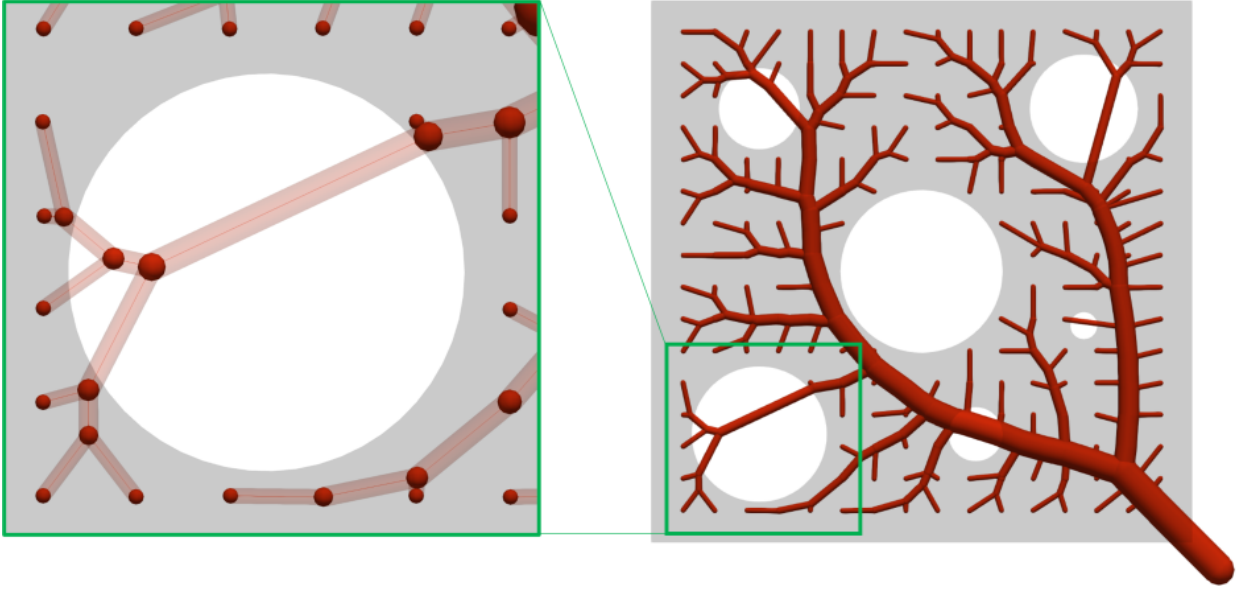


Figure 3: Vascular tree inside a nonconvex perfusion volume (grey, rectangular shape with six “holes”). Left side: Even with terminal nodes sampled inside Ω , branching nodes (red spheres) and edges (shaded connections) can be synthesized outside Ω .

We assume that Ω is given by its boundary $\partial\Omega$, a closed surface consisting of finitely many triangles. Such a *triangulation* is a standard discretization of the physical volume’s boundary. It enables cheap computations of many geometric properties, such as testing whether a given point belongs to Ω or determining its distance to $\partial\Omega$. All the data sets that we consider in this work represent $\partial\Omega$ (and thus Ω) by a sufficiently fine triangulation. With this assumption for Ω , we can generate all terminal nodes uniformly inside Ω at the start of the algorithm. We sample all points inside the bounding box of Ω on some regular grid (with the addition of small random perturbations) and, subsequently, delete each point outside Ω . By choosing the density of the grid based on the volume ratio between bounding box and Ω , the final sample size N_{term} only deviates slightly from the desired number of terminals.

Now, given a nonconvex domain Ω , we first solve the NLP (14)–(16) to synthesize an initial vascular tree that will typically not lie entirely in Ω . Instead of introducing local changes to individually move nodes and segments inside Ω , our goal is then to achieve this by repeating our global geometry optimization with additional constraints. To this end, we compute the set \mathbb{V}_{ext} of tree nodes outside Ω and the set \mathbb{A}_{ext} of segments that pass through the exterior of Ω even though both its proximal and distal nodes are already inside. For every node $v \in \mathbb{V}_{\text{ext}}$, we set $c_v := x_v$ (the node’s infeasible location) and $d_v := \text{dist}(c_v, \partial\Omega)$ (its distance to the boundary). Then we extend the original NLP with a constraint that excludes the open ball $B(c_v, d_v + \varepsilon_v) := \{x: \|x - c_v\| < d_v + \varepsilon_v\}$ from the feasible region for x_v , where the parameter ε_v is chosen to be larger than the largest segment radius at node v . For every segment $a = uv \in \mathbb{A}_{\text{ext}}$, we determine the

point c_a on the line segment $[x_u, x_w]$ that has the largest distance d_a to $\partial\Omega$. Then we add an *extension node* $v \equiv v_a$ (originally located at c_a) to split the segment $a = uw$ into two parts uv and vw that may form a kink, and we extend the original NLP with a constraint that excludes the open ball $B(c_a, d_a + \varepsilon_a)$ from the feasible region for x_v and with constraints that prevent a shortening of the two new segments. The parameter ε_a is chosen to be larger than the segment radius r_a . We denote by $\mathbb{E} := \{v_a : a \in \mathbb{A}_{\text{ext}}\}$ the set of extension nodes and by $\mathbb{B} := \mathbb{V}_{\text{ext}} \cup \mathbb{E}$ the set of nodes with ball constraints and by $\mathbb{A}_{\mathbb{E}} := \bigcup_{uw \in \mathbb{A}_{\text{ext}}} \{uv_a, v_a w\}$ the set of split arc pairs. For $v \equiv v_a \in \mathbb{E}$ with $a = uw$ we write c_v, d_v, ε_v instead of c_a, d_a, ε_a , and we set $\bar{\ell}_{uv} := \|x_u - c_v\|$ and $\bar{\ell}_{vw} := \|c_v - x_w\|$. Our variable vector y now also includes the location x_v of each extension node, its distance ℓ_v to the associated ball center c_v , and the lengths ℓ_{uv}, ℓ_{vw} of split arc pairs. The best geometry (inside the nonconvex volume) is then found in

$$Y = \mathbb{R}^{3|\mathbb{V}|+3|\mathbb{E}|+|\mathbb{B}|} \times [\ell^-, \ell^+]^{|\mathbb{A}|+|\mathbb{A}_{\text{ext}}|+|\mathbb{B}|}, \quad (17)$$

and the extended NLP reads:

$$\min_{y \in Y} \sum_{a \in \mathbb{A}} \ell_a w_a(r_a) \quad (18)$$

$$\text{s.t. } 0 = x_u - \bar{x}_u, \quad u \in \{0\} \cup \mathbb{L}, \quad (19)$$

$$0 = \ell_{uv}^2 - \|x_u - x_v\|^2, \quad uv \in \mathbb{A} \setminus \mathbb{A}_{\text{ext}} \cup \mathbb{A}_{\mathbb{E}}, \quad (20)$$

$$0 = \ell_v^2 - \|x_v - c_v\|^2, \quad v \in \mathbb{B}, \quad (21)$$

$$\ell_v \geq d_v + \varepsilon_v, \quad v \in \mathbb{B}, \quad (22)$$

$$\ell_{uv} \geq \bar{\ell}_{uv}, \ell_{vw} \geq \bar{\ell}_{vw}, \quad v \in \mathbb{E}, uw \in \mathbb{A}_{\text{ext}}. \quad (23)$$

Clearly, (21) defines the length ℓ_v and (22) forces each node in \mathbb{B} outside its corresponding ball (by a tolerance distance ε_v). Smaller values of ε_v lead to more “natural” (near-optimal) vessel curvature while increasing the number of extension nodes that need to be added, as highlighted in Fig. 4 for a common value of ε at all nodes. The two last constraints (23) prevent extension nodes from moving closer to either their proximal or distal node and, instead, to form a kink while moving outside their corresponding ball.

Remark 6.1: The radius of a segment uw only depends on the number of leaf nodes downstream of node w . Thus, adding an extension node v on segment uw does not change the radii for the new segments uv and vw , which are both equal to r_{uw} .

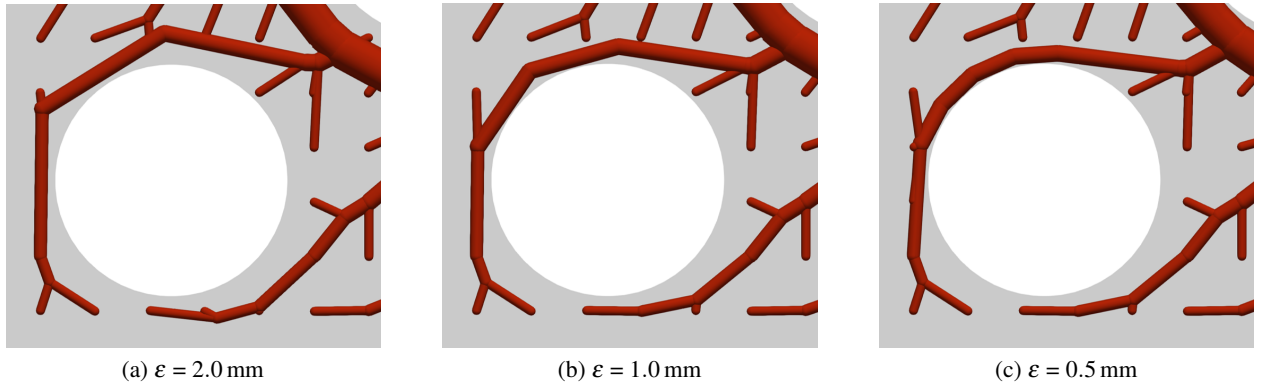


Figure 4: Influence of the allowed minimum distance ε between balls and nodes of the tree. Smaller values of ε lead to more optimal geometry (tighter curves) at the expense of additional extension nodes.

The (general) detection of nodes outside the perfusion volume and the computation of the initial extension locations can not be formulated as NLP constraints. Therefore these operations must be executed outside (before) solving the NLP. The result is an iterative approach wherein we repeatedly detect and add new extensions to optimize the global geometry constrained to the nonconvex perfusion volume until all segments lie entirely inside Ω . This process is visualized in Fig. 5 and the complete algorithm is summarized in Algorithm 1.

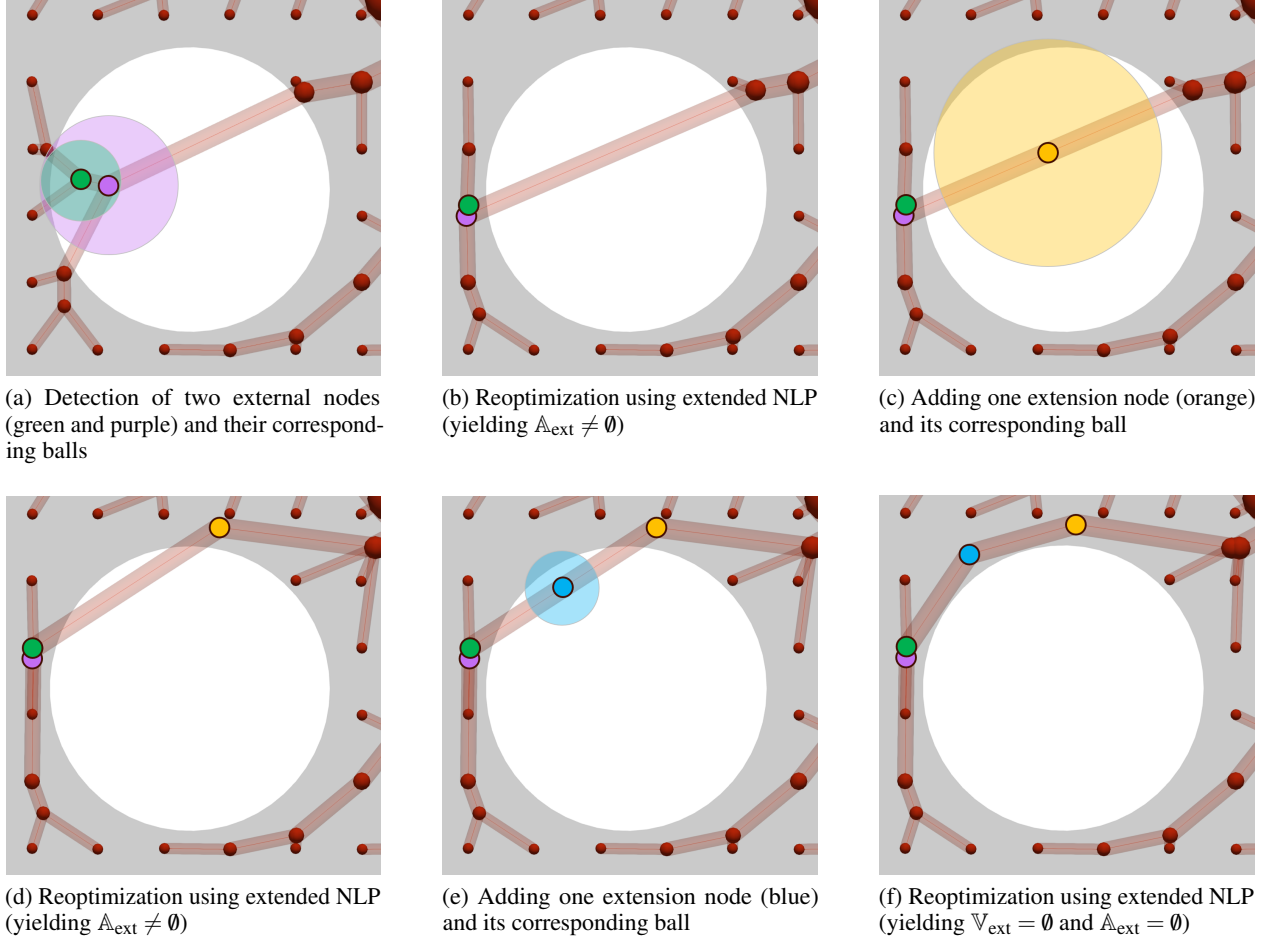


Figure 5: Steps to constrain a vascular tree inside a nonconvex perfusion volume Ω . To resolve this section of Ω , a total of two new extension nodes are added.

Algorithm 1 Nonconvex algorithm

- 1: Compute an initial tree using the NLP (14)–(16)
 - 2: Compute the sets \mathbb{V}_{ext} and \mathbb{A}_{ext}
 - 3: **while** $\mathbb{V}_{\text{ext}} \neq \emptyset$ or $\mathbb{A}_{\text{ext}} \neq \emptyset$ **do**
 - 4: Add extension nodes to the segments in \mathbb{A}_{ext}
 - 5: Identify the set of nodes with ball constraints \mathbb{B}
 - 6: Reoptimize the tree geometry using the NLP (18)–(23)
 - 7: Recompute the sets \mathbb{V}_{ext} and \mathbb{A}_{ext}
 - 8: **end while**
-

2.3.3 Extension to multiple non-intersecting trees

The perfusion of an organ involves at least two vascular trees (with common terminal nodes); typically one inlet and one outlet tree. However, without additional constraints, two generated trees inside the same perfusion domain face a high risk of intersecting each other, as highlighted in Fig. 6. Similar to the treatment of nonconvexity, our proposed approach for removing any intersections consists in synthesizing multiple vascular trees independently in a first step and repeating our NLP-based global geometry optimization with appropriate additional constraints. Every reoptimization step in this process combines the global geometry models of all trees along with all added non-intersection constraints in a single extended NLP.

To identify intersections efficiently, we treat each segment as a capsule, i.e., as a cylinder with a half-ball attached to each end; see Fig. 7. The intersection test between two segments then consists of two parts. The first is finding the pair of nearest points on the two cylinder axes (line segments). The second part is to test whether the distance between these two nearest points is smaller than the combined radii of both capsules. We further accelerate the identification of intersections by utilizing appropriate bounding boxes. Based on this identification, [12] proposed a local algorithm to remove intersections by introducing extension nodes at the locations of intersections and moving them apart based on their intersection depth. This algorithm can remove any intersection, but it introduces a large number of extension nodes, even for larger vessels. The result is a significant increase in metabolic cost and an unnaturally high curvature of modified vessels.

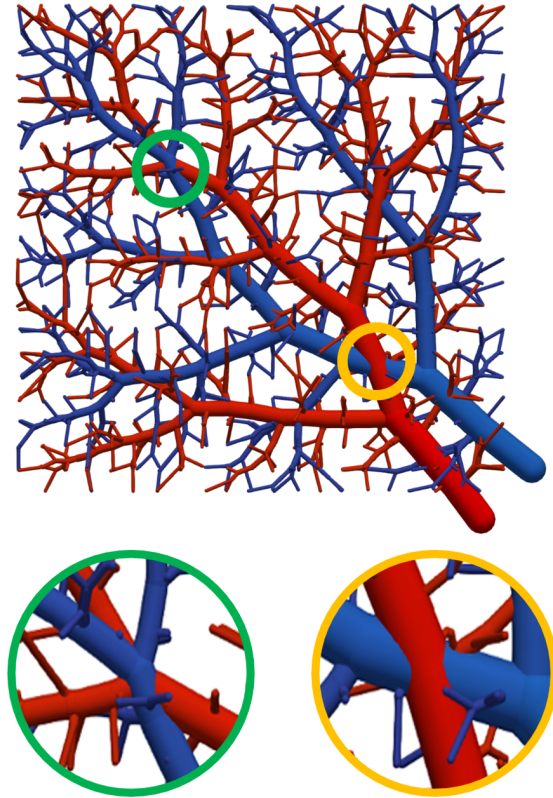


Figure 6: Two vascular trees generated in the same perfusion volume Ω . Without additional constraints, these trees can penetrate each other. Two intersections are highlighted in green and orange. The two trees intersect a total of 31 times (total tree energy 4334).

By allowing all nodes to move, both the number of extension nodes and the increase in cost should be significantly reduced with our reoptimization approach. Since the first part of the intersection test can not

be formulated as NLP constraints, we can only include the second part. Therefore the identification of the closest points (and addition as extension nodes) must be performed before solving the NLP, which results in an iterative approach similar to Algorithm 1.

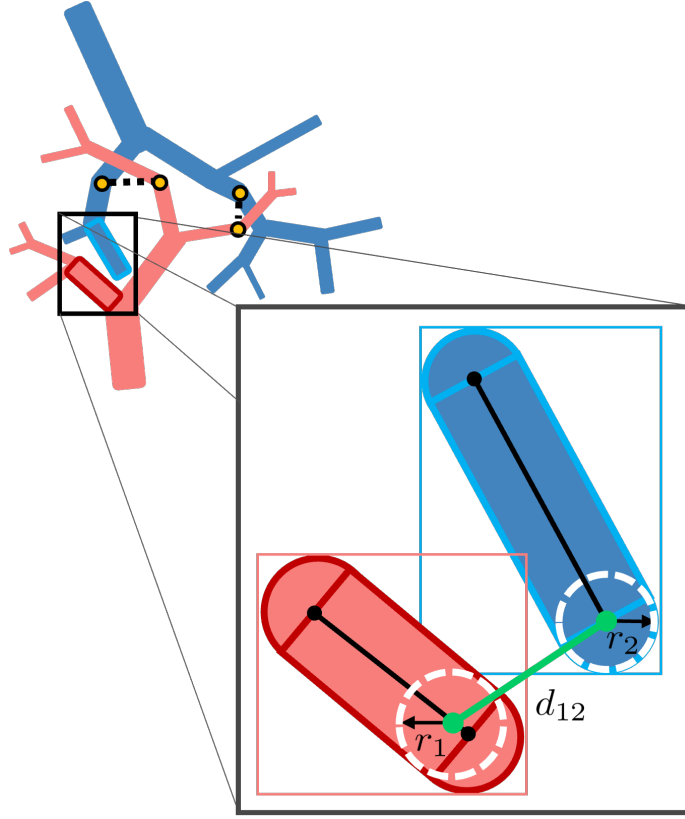


Figure 7: Steps to identify and remove intersecting vessels. Bounding boxes and capsules are used to find intersections. New extension nodes (orange) are introduced to remove these intersections.

For the reoptimization, we consider a *forest* consisting of any number $N_{\mathbb{T}}$ of trees $\mathbb{T}_i = (\mathbb{V}_i, \mathbb{A}_i)$, represented by its index set

$$\mathbb{F} = \{1, \dots, N_{\mathbb{T}}\}. \quad (24)$$

We check for intersections inside the forest pairwise with

$$\mathbb{P} = \{(i, j) : i, j \in \mathbb{F}, i < j\} \quad (25)$$

and introduce for each tree pair $(i, j) \in \mathbb{P}$ the set of all pairs (a_i, a_j) of intersecting segments along with their associated nearest points (c_i, c_j) ,

$$\mathbb{A}_{ij} = \{(a_i, a_j, c_i, c_j) : (a_i, a_j) \in \mathbb{A}_i \times \mathbb{A}_j \text{ intersect}\}. \quad (26)$$

Every quadruple in \mathbb{A}_{ij} with $a_i = u_i w_i$ and $a_j = u_j w_j$ therefore has $c_i \in [u_i, w_i]$ and $c_j \in [u_j, w_j]$ such that

$$\text{dist}([u_i, w_i], [u_j, w_j]) = \|c_i - c_j\| < r_{a_i} + r_{a_j}. \quad (27)$$

We define parameters $\bar{\ell}_{u_i c_i} := \|x_{u_i} - c_i\|$ and $\bar{\ell}_{c_i w_i} := \|c_i - x_{w_i}\|$, and similarly for c_j . Our variable vector y now includes the variables of all individual trees as well as the locations x_{v_i}, x_{v_j} of the extension nodes (initially

set to c_i, c_j) with associated lengths ℓ_{v_i}, ℓ_{v_j} , and the lengths $\ell_{u_i v_i}, \ell_{v_i w_i}$ of split arc pairs. Using the union $\mathbb{A}_{\mathbb{P}} := \bigcup_{(i,j) \in \mathbb{P}} \mathbb{A}_{ij}$, the extended NLP then becomes:

$$\min_{y \in Y} \sum_{i \in \mathbb{F}} \sum_{a_i \in \mathbb{A}_i} \ell_{a_i} w_{a_i} (r_{a_i}) \quad (28)$$

$$\text{s.t. } 0 = x_{u_i} - \bar{x}_{u_i}, \quad i \in \mathbb{F}, u_i \in \{\mathbf{0}\}_i \cup \mathbb{L}, \quad (29)$$

$$0 = \ell_{u_i v_i}^2 - \|x_{u_i} - x_{v_i}\|^2, \quad i \in \mathbb{F}, u_i v_i \in \mathbb{A}_i, \quad (30)$$

$$0 = \ell_{v_i v_j}^2 - \|x_{v_i} - x_{v_j}\|^2, \quad (a_i, a_j, v_i, v_j) \in \mathbb{A}_{\mathbb{P}}, \quad (31)$$

$$\ell_{v_i v_j} \geq r_{a_i} + r_{a_j} + \varepsilon, \quad (a_i, a_j, v_i, v_j) \in \mathbb{A}_{\mathbb{P}}, \quad (32)$$

$$\ell_{u_i v_i} \geq \bar{\ell}_{u_i c_i}, \ell_{u_i v_j} \geq \bar{\ell}_{u_i c_j}, \quad (a_i, a_j, v_i, v_j) \in \mathbb{A}_{\mathbb{P}}, \quad (33)$$

$$\ell_{v_i w_i} \geq \bar{\ell}_{c_i w_i}, \ell_{v_j w_j} \geq \bar{\ell}_{c_j w_j}, \quad (a_i, a_j, v_i, v_j) \in \mathbb{A}_{\mathbb{P}}. \quad (34)$$

Herein (31) defines the distance between a pair of extension nodes of two trees and (32) ensures that the associated segments do not overlap at these nodes (with a tolerance ε). As for the nonconvex volume, (33) and (34) force segments with extension nodes to develop kinks. To completely remove all intersections, we need to iterate between adding new extension nodes at intersections and solving the NLP, as shown in Algorithm 2. Figure 8 highlights how this approach iteratively removes all intersections.

Algorithm 2 No-intersection algorithm

- 1: Compute $N_{\mathbb{T}}$ initial trees independently
 - 2: Detect and count the number of intersections N
 - 3: **while** $N > 0$ **do**
 - 4: Add extension nodes to intersecting segments
 - 5: Identify the set \mathbb{A}_{ij} for each tree pair in the forest
 - 6: Reoptimize the tree geometry using the NLP (28)–(34)
 - 7: Detect and count the number of intersections N
 - 8: **end while**
-

2.4 Complete framework

We combine our geometry optimization algorithms with the SA algorithm, introduced in [8], into a unified generation framework that is capable of generating vascular trees up to the micro-circulation. The generation of the trees starts by sampling the N_{term} common terminal nodes inside Ω based on the choice of distribution. From this set of terminal nodes, N_{topo} nodes are randomly sampled and the topology of each tree is optimized (with the same N_{topo} nodes) as described in [8]. The geometry of the resulting locally optimal topology is then globally optimized and constrained to adhere to (possibly) nonconvex perfusion volumes and multiple trees, according to Algorithm 1 and Algorithm 2. Afterward, the number of current terminal nodes is doubled (sampled from the initial N_{term} terminal nodes). To avoid unnecessary intersections, we reject samples inside already existing vessels. From here, the SA algorithm starts again.

During our tests, this process resulted in a good balance between computational complexity and optimality of the final trees. After all terminals are connected, the trees can be reoptimized again to adhere to more complicated physiological phenomena, such as non-Newtonian blood rheology [15]. Lastly, any segments that reach the lower length bound ℓ^- are considered degenerate and are removed and replaced with their branch segments, possibly creating n -furcations with $n \geq 3$. This complete generation framework is shown in Algorithm 3.

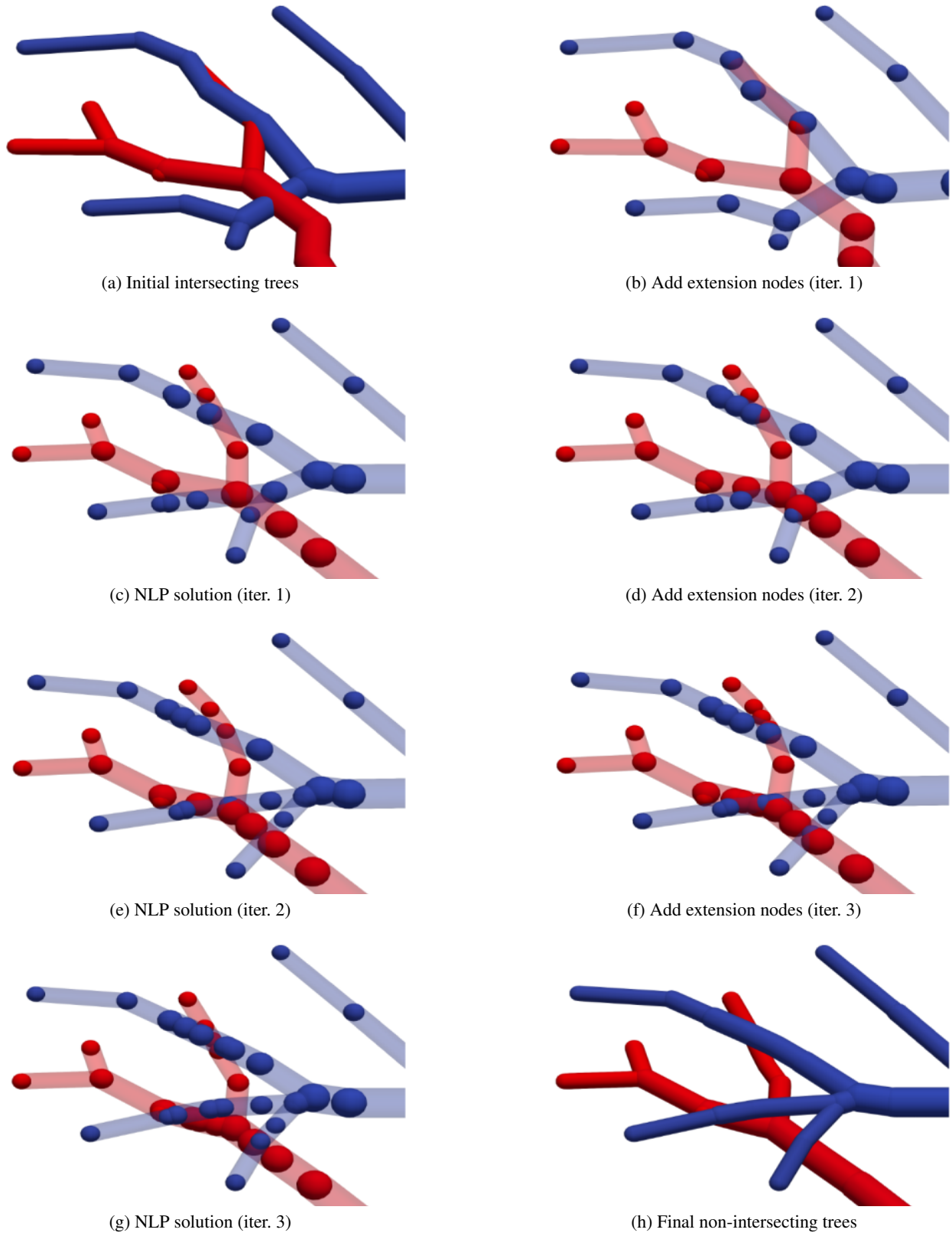


Figure 8: Steps to (globally) remove intersections between two vascular trees.

Algorithm 3 Complete generation framework

```

1: Sample  $N_{\text{term}}$  terminal nodes inside  $\Omega$ 
2: Create  $N_{\text{T}}$  initial trees sharing  $N = N_{\text{topo}}$  terminal nodes
3: while  $N < N_{\text{term}}$  do
4:   Optimize trees using SA algorithm of [8]
5:   Apply Algorithm 1 and/or Algorithm 2 (as needed)
6:   Set  $M = \min(2N, N_{\text{term}})$ 
7:   for  $i = N + 1, \dots, M$  do
8:     if node  $x_{\text{term},i}$  outside existing vessels then
9:       Connect node  $x_{\text{term},i}$  to nearest edge
10:    end if
11:  end for
12:  Set  $N = M$ 
13: end while
14: Apply Algorithm 1 and/or Algorithm 2 (as needed)
15: Replace degenerate segments with proximal node

```

3 Results

3.1 Implementation details

Our framework is implemented in the programming language *Julia* [18]. The NLPs are solved using an interior point method implemented in the program *Ipopt* [19] together with the linear solver *Mumps* [20]. All computations, including the reference benchmarks, were done on a desktop computer with 64 GB of random-access memory (RAM) and an AMD Ryzen 7950x @5Ghz CPU with 32 processing threads.

3.2 Rectangle domain with holes

We start by restricting a single vascular tree to the nonconvex domain introduced with Fig. 3. The excluded domain consists of six differently sized holes, with diameters ranging from 2 mm to 25 mm. The resulting constrained tree is shown in Fig. 9 in red against the initial unconstrained tree in green. All vessels and nodes are moved inside the domain (grey). The largest difference in geometry to the initial tree is in the vicinity of the holes. Because we consider the global geometry, we also see differences in other areas of the tree. Most notably, the vessels of the left trunk behind the first major branch point moved slightly upwards to alleviate the following kink near the bottom center hole. The energy cost of the tree increased by 2.5% with a total of 8 extension nodes introduced.

3.3 Two trees inside rectangle

In the second example, we consider the two intersecting trees of Fig. 6. Each tree consists of 1,000 nodes and the combined tree energy is 4,334. Without additional constraints, the trees intersect a total of 31 times. The result of our new global algorithm is shown in Fig. 10 (right side) against the local algorithm, proposed in [12] (left side). While both approaches remove all intersections, the local one produces a large number of extension nodes and an “unnaturally” high curvature of larger vessels. In comparison, our algorithm avoids most intersections by simply moving the branching nodes of the red tree behind the blue tree. Thus, the cost increases only by around 0.4% (using 11 extension nodes) compared to the local approach with a 2.4% cost increase (using 53 extension nodes).

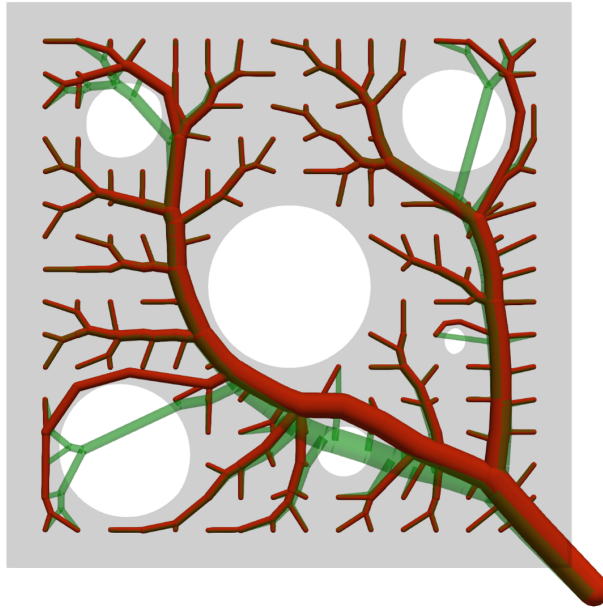


Figure 9: Vascular tree in red after optimization with additional constraints to keep the tree inside Ω . The initial (unconstrained) tree is shown in green.

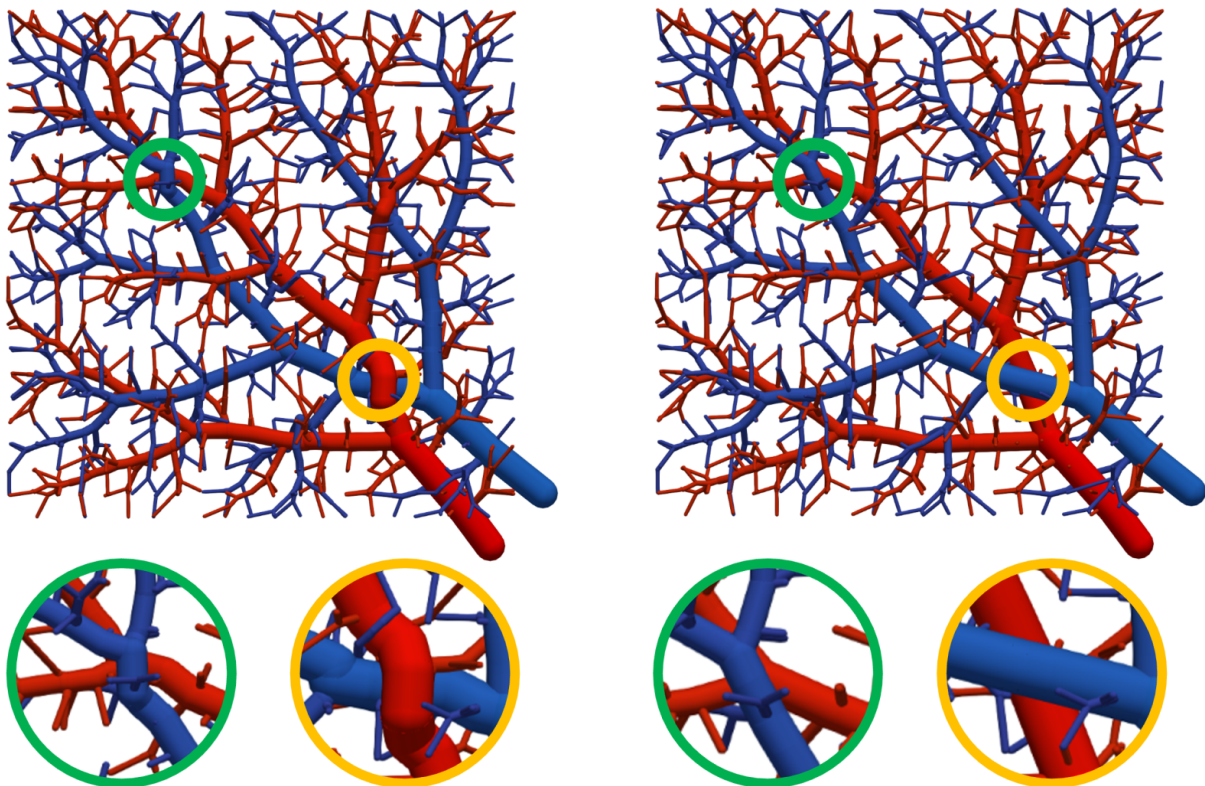


Figure 10: Comparison of the local intersection removal (left) and our new global algorithm (right). Both algorithms remove all intersections as highlighted in green and orange. The local algorithm needs 53 extension nodes (total tree energy 4438) while the global algorithm needs only 11 extension nodes (total tree energy 4352). The intersecting trees have total energy 4334.

3.4 Brain: Left frontal gyrus

To test how our framework handles multiple trees inside a domain with severe nonconvex features, we choose the left frontal gyrus of the human brain. Its geometric definition is based on a human brain reconstruction from the BodyParts3D database [21]. We generated one inflow and one outflow tree with 50,000 terminal vessels each. The gyrus volume and the final generated tree are shown in Fig. 11. Both trees are constrained inside the nonconvex domain and do not intersect. Moreover, no unnatural branches are introduced as in local approaches [12]. Both generated trees reproduce several architectural features observed in experimental studies [22–24]. Firstly, the root quickly branches into two vessels, which supply the left and right sides of the gyrus. Furthermore, because the root nodes of both trees are close to each other, the largest vessels run parallel to each other.

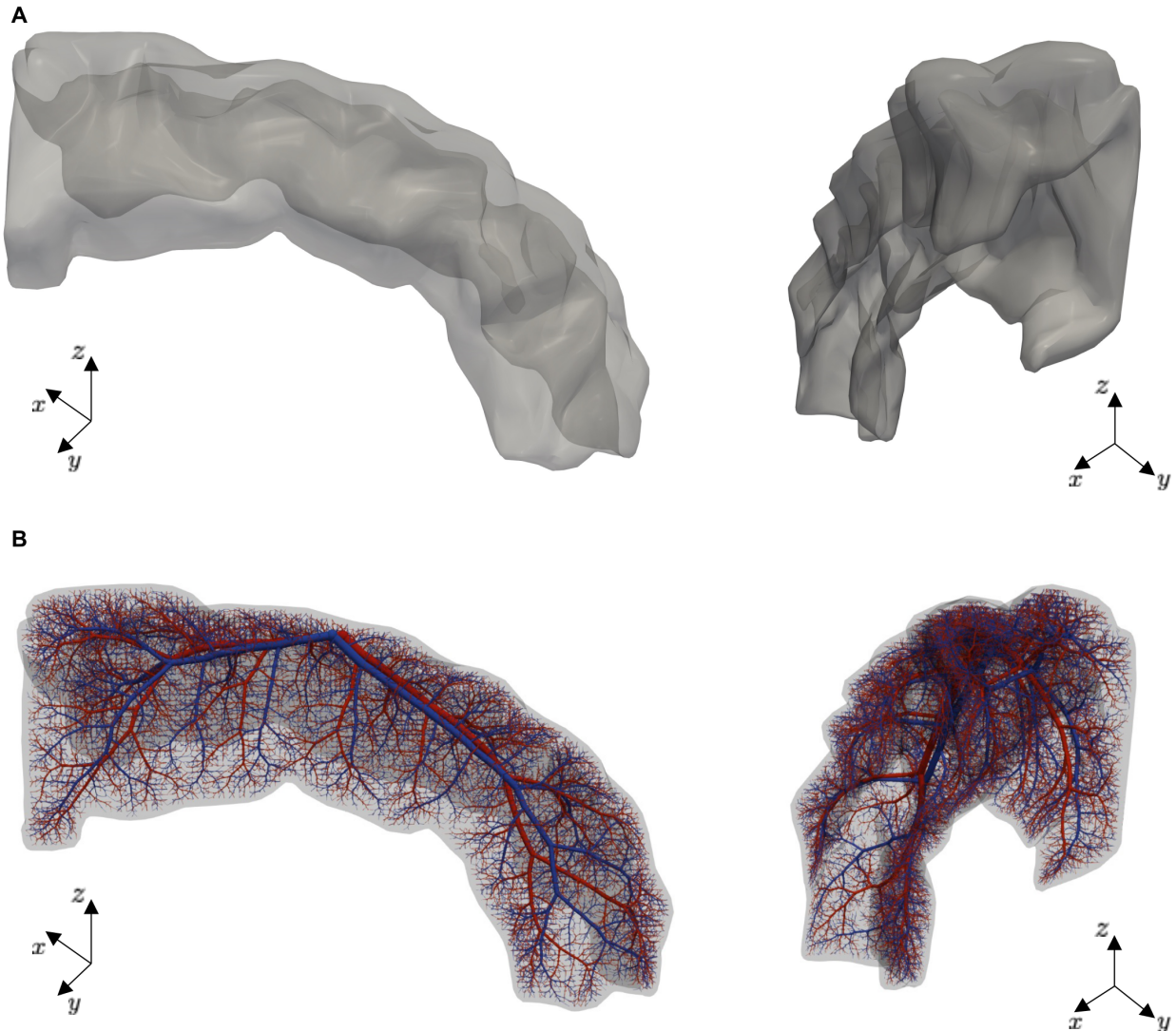


Figure 11: Generation of supplying and draining vascular trees inside a replica of the anatomic brain part of the left gyroid. **(a)** Front and side view of the left gyroid, highlighting the nonconvex features of the organ part. **(b)** Resulting vascular trees with $N_{\text{term}} = 50,000$ terminal nodes. Our new algorithm keeps both trees inside the gyroid without penetration and without introducing (unphysical) extensions.

3.5 Liver: Full-scale hepatic trees

As a final example, we consider the hepatic vascular systems of the human liver. In comparison to the brain, the liver has an almost convex shape (unless we exclude the gallbladder). However, in contrast to other organs, the liver has two supplying trees. The first one is supplied through the *hepatic artery* (HA) from the heart, and the second one is supplied through the *portal vein* (PV) from the digestive tract. The blood leaves the liver through a single draining tree into the *hepatic veins* (HV) leading into the vena cava inferior (VCI). The synthetic generation of the hepatic vasculature is based on the perfusion volume of the experimentally investigated trees from Debbaut et al. [25]. The physiological parameters are taken from Kretowski et al. [7]; see Table 1. We generate the vascular trees with $N_{\text{term}} = 100,000$ (matched) terminal nodes.

Table 1: Model parameters used to generate the synthetic vascular trees of PV, HV and HA

Parameter	Description	Units	Value (PV, HV, HA)
Ω	Perfusion volume	mm^3	1500
\mathbb{T}_k	Initial tree	—	Root and vessels of depth $k \leq 2$
Q_{perf}	Root flow	$\text{mm}^3 \text{s}^{-1}$	(16.5, 20.0, 3.5)
N_{term}	Number of terminal nodes	1	100,000
m_b	Metabolic demand factor of blood	$\mu\text{W mm}^{-3}$	(0.4, 0.2, 0.65)
η_p	Blood viscosity	cP	3.6

The final hepatic vasculature is depicted in Fig. 12, showing both the coupled vasculature, Fig. 12 (A), and the individual trees from multiple viewpoints, Fig. 12 (B–E). We can recover multiple topological features of real hepatic vasculature trees, most notably, the parallel development of PV and PA vessels after the first two generations and the tendency of the smaller vessels (mainly from PA) to wrap around the larger vessels.

4 Conclusion

In this paper, we extended our previous framework to generate multiple trees inside general nonconvex perfusion volumes. We approximate regions that need to be excluded by a set of medial balls and introduce distance constraints to neighboring tree nodes. Similar distance criteria are introduced for neighboring nodes of different trees. We include both constraint types in our global geometry optimization. In contrast to local approaches, we accommodate these constraints in the global tree geometry. This results in more natural vessel curvature and, subsequently, reduced metabolic cost.

We tested our approach for the vasculature inside the left frontal gyroid of the human brain and the vasculature inside the human liver. In both cases, we can reproduce key physiological features such as the parallel vessel paths of the larger vessels and the tortuous shapes of smaller vessels.

While our NLP extension improves the comparison to in-vivo data, our underlying assumptions limit applicability to the pre-capillary level. On the capillary level, the structure transmutes from pure branching to a meshed network. This is outside the scope of our topology modeling.

We expect that our framework could be helpful in several applications. Firstly, synthetic trees generated by this framework could help to improve the interpretation of medical images by, e.g., artificially increasing the density of the initial segmented tree to the desired pre-capillary level. Such dense trees could improve the functional assessment of organs such as the liver [26]. One specific case is the understanding of why vessels become tortuous. We can reproduce several observed shapes purely based on intersection avoidance. Another

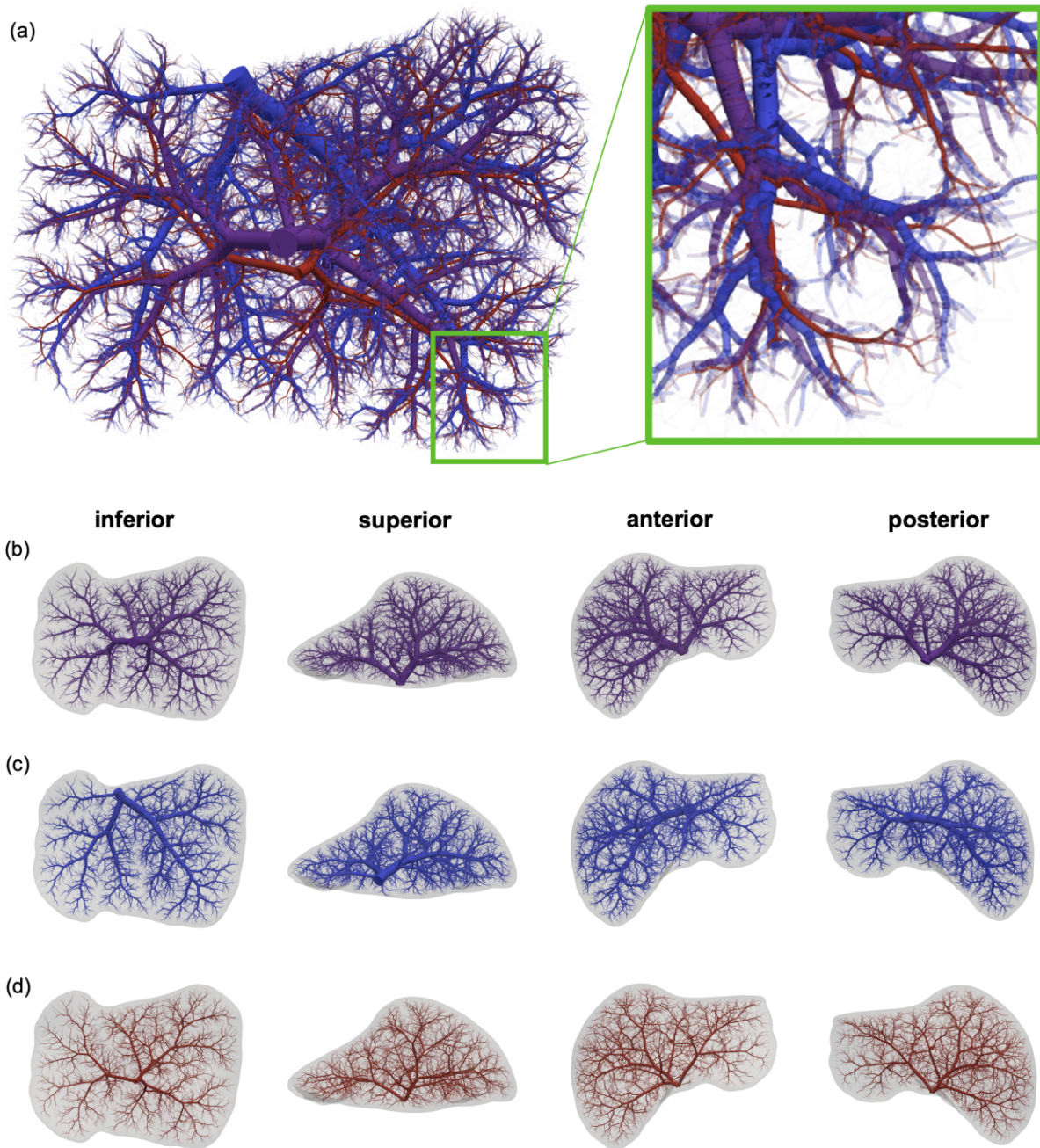


Figure 12: Synthetic hepatic vasculature (PV, HV, PA) generated with our optimization framework. Each tree consists of 100,000 terminal vessels. **(a)** Complete vasculature from inferior view with two zoom levels highlighting the different scales. **(b)–(d)** Individual trees inside perfusion volume (grey) shown from different views: **(b)** PV, **(c)** HV and **(d)** HA.

application includes the field of tissue-engineered products [27]. Here, tissue is bio-printed and requires (ideally optimal) vascular trees to support its cells. Our framework would allow us to construct supplying and draining trees under different design goals and constraints.

Acknowledgment

The results presented in this paper were obtained as part of the ERC Starting Grant project “ImageToSim” that has received funding from the European Research Council (ERC) under the European Union’s Horizon 2020 research and innovation programme (Grant agreement No. 759001). The authors gratefully acknowledge this support.

References

- [1] A. Noordergraaf, *Circulatory System Dynamics*, vol. 1. Elsevier, 2012.
- [2] N. Sakalihasan, R. Limet, and O. D. Defawe, “Abdominal aortic aneurysm,” *The Lancet*, vol. 365, no. 9470, pp. 1577–1589, 2005.
- [3] R. Bonita, “Epidemiology of stroke.,” *The Lancet*, vol. 339, no. 8789, pp. 342–344, 1992.
- [4] W. Schreiner and P. F. Buxbaum, “Computer-optimization of vascular trees,” *IEEE Transactions on Biomedical Engineering*, vol. 40, no. 5, pp. 482–491, 1993.
- [5] R. Karch, F. Neumann, M. Neumann, and W. Schreiner, “A three-dimensional model for arterial tree representation, generated by constrained constructive optimization,” *Computers in Biology and Medicine*, vol. 29, no. 1, pp. 19–38, 1999.
- [6] L. O. Schwen and T. Preusser, “Analysis and algorithmic generation of hepatic vascular systems,” *International journal of hepatology*, vol. 2012, 2012.
- [7] M. Kretowski, Y. Rolland, J. Bézy-Wendling, and J.-L. Coatrieux, “Physiologically based modeling of 3-d vascular networks and ct scan angiography,” *IEEE transactions on medical imaging*, vol. 22, no. 2, pp. 248–257, 2003.
- [8] E. Jessen, M. C. Steinbach, C. Debbaut, and D. Schillinger, “Rigorous mathematical optimization of synthetic hepatic vascular trees,” *Journal of the Royal Society Interface*, vol. 19, no. 191, p. 20220087, 2022.
- [9] Z. A. Sexton, A. R. Hudson, J. E. Herrmann, D. J. Shiwarski, J. Pham, J. M. Szafron, S. M. Wu, M. Skylar-Scott, A. W. Feinberg, and A. Marsden, “Rapid model-guided design of organ-scale synthetic vasculature for biomanufacturing,” *arXiv preprint arXiv:2308.07586*, 2023.
- [10] G. D. M. Talou, S. Safaei, P. J. Hunter, and P. J. Blanco, “Adaptive constrained constructive optimisation for complex vascularisation processes,” *Scientific Reports*, vol. 11, no. 1, p. 6180, 2021.
- [11] L. Cury, G. Maso Talou, M. Younes-Ibrahim, and P. Blanco, “Parallel generation of extensive vascular networks with application to an archetypal human kidney model,” *Royal Society Open Science*, vol. 8, no. 12, p. 210973, 2021.
- [12] A. A. Guy, A. W. Justin, D. M. Aguilar-Garza, and A. E. Markaki, “3d printable vascular networks generated by accelerated constrained constructive optimization for tissue engineering,” *IEEE Transactions on Biomedical Engineering*, vol. 67, no. 6, pp. 1650–1663, 2019.

- [13] H. K. Hahn, M. Georg, and H.-O. Peitgen, “Fractal aspects of three-dimensional vascular constructive optimization,” in *Fractals in biology and medicine*, pp. 55–66, Springer, 2005.
- [14] J. Keelan, E. M. Chung, and J. P. Hague, “Simulated annealing approach to vascular structure with application to the coronary arteries,” *Royal Society open science*, vol. 3, no. 2, p. 150431, 2016.
- [15] E. Jessen, M. C. Steinbach, C. Debbaut, and D. Schillinger, “Branching exponents of synthetic vascular trees under different optimality principles,” *IEEE Transactions on Biomedical Engineering*, vol. 71, no. 4, pp. 1345–1354, 2023.
- [16] C. D. Murray, “The physiological principle of minimum work: I. The vascular system and the cost of blood volume,” *Proceedings of the National Academy of Sciences of the United States of America*, vol. 12, no. 3, p. 207, 1926.
- [17] Y. Liu and G. S. Kassab, “Vascular metabolic dissipation in Murray’s law,” *American Journal of Physiology-Heart and Circulatory Physiology*, vol. 292, no. 3, pp. H1336–H1339, 2007.
- [18] J. Bezanson, A. Edelman, S. Karpinski, and V. B. Shah, “Julia: A fresh approach to numerical computing,” *SIAM Review*, vol. 59, no. 1, pp. 65–98, 2017.
- [19] A. Wächter and L. T. Biegler, “On the implementation of an interior-point filter line-search algorithm for large-scale nonlinear programming,” *Mathematical Programming*, vol. 106, no. 1, pp. 25–57, 2006.
- [20] P. R. Amestoy, I. S. Duff, J. Koster, and J.-Y. L’Excellent, “A fully asynchronous multifrontal solver using distributed dynamic scheduling,” *SIAM J. Matrix Anal. Appl.*, vol. 23, no. 1, pp. 15–41, 2001.
- [21] “BodyParts3D - The Database Center for Life Science.” <http://lifesciencedb.jp/bp3d>, 2024. [Online; accessed 19-April-2024].
- [22] H. M. Duvernoy, S. Delon, and J. Vannson, “Cortical blood vessels of the human brain,” *Brain research bulletin*, vol. 7, no. 5, pp. 519–579, 1981.
- [23] F. Lauwers, F. Cassot, V. Lauwers-Cances, P. Puwanarajah, and H. Duvernoy, “Morphometry of the human cerebral cortex microcirculation: general characteristics and space-related profiles,” *Neuroimage*, vol. 39, no. 3, pp. 936–948, 2008.
- [24] F. Cassot, F. Lauwers, S. Lorthois, P. Puwanarajah, V. Cances-Lauwers, and H. Duvernoy, “Branching patterns for arterioles and venules of the human cerebral cortex,” *Brain research*, vol. 1313, pp. 62–78, 2010.
- [25] C. Debbaut, P. Segers, P. Cornillie, C. Casteleyn, M. Dierick, W. Laleman, and D. Monbaliu, “Analyzing the human liver vascular architecture by combining vascular corrosion casting and micro-CT scanning: A feasibility study,” *Journal of Anatomy*, vol. 224, no. 4, pp. 509–517, 2014.
- [26] B. Vollmar and M. D. Menger, “The hepatic microcirculation: mechanistic contributions and therapeutic targets in liver injury and repair,” *Physiological reviews*, vol. 89, no. 4, pp. 1269–1339, 2009.
- [27] G. A. Salg, A. Blaeser, J. S. Gerhardus, T. Hackert, and H. G. Kenngott, “Vascularization in bioartificial parenchymal tissue: bioink and bioprinting strategies,” *International Journal of Molecular Sciences*, vol. 23, no. 15, p. 8589, 2022.